

# The Forward Tagger for CLAS12

M. Bashkanov<sup>h</sup>, M.Battaglieri<sup>a,\*</sup>, A. Bersani<sup>a</sup>, A. Casale<sup>a</sup>, A. Celentano<sup>a</sup>, R. Cereseto<sup>a</sup>, F. Cipro<sup>a</sup>, R. De Vita<sup>a</sup>, E. Fanchini<sup>a</sup>, S. Fegan<sup>f</sup>, J. Flemming<sup>i</sup>, S. Hughes<sup>i</sup>, G. Min<sup>a</sup>, P. Musico<sup>a</sup>, M. Osipenko<sup>a</sup>, G. Ottonello<sup>a</sup>, F. Parodi<sup>a</sup>, F. Pratolongo<sup>a</sup>, R. Puppo<sup>a</sup>, M. Ripani<sup>a</sup>, G. Smith<sup>i</sup>, I. Stankovic<sup>i</sup>, M. Taiuti<sup>a,d</sup>, D. Watts<sup>h</sup>, N. Zachariou<sup>h</sup>, L. Zana<sup>f</sup>, add authors from other institutions

<sup>a</sup>INFN - Sezione di Genova, Via Dodecaneso 33, I-16146 Genova, Italy

<sup>b</sup>INFN, Sezione di Roma Tor Vergata, 00133 Rome, Italy

<sup>c</sup>INFN, Sezione di Torino, 10125 Torino, Italy

<sup>d</sup>Università degli Studi di Genova, Via Dodecaneso 33, I-16146 Genova, Italy

<sup>e</sup>Università di Roma Tor Vergata, 00133 Rome, Italy

<sup>f</sup>Jefferson Lab, Newport News, VA 23606, USA

<sup>g</sup>IRFU, CEA, Université Paris-Saclay, F-91191 Gif-sur-Yvette, France

<sup>h</sup>University of York, York YO10 5DD, United Kingdom

<sup>i</sup>University of Edinburgh, Edinburgh EH9 3FD, United Kingdom

---

## Abstract

This document presents the technical layout and the performance of the CLAS12 Forward Tagger (FT). The FT, composed by an electromagnetic calorimeter based on PbWO crystals (FT-Cal) a scintillation hodoscope (FT-Hodo) and several layers of Micromegas trackers (FT-Trck), has been designed to detect electrons and photons scattered at very small angles and meet the physics goals of the hadron spectroscopy program and other experiments running with CLAS12 in Hall-B.

**Keywords:** Hadron spectroscopy, Low- $Q^2$  electron scattering, Electromagnetic calorimeter, PbWO<sub>4</sub>, APD, hodoscope, plastic scintillator, WLS fibers, SiPM, gas tracking detector, MicroMegas

---

## 1. Introduction

An experimental program focused on search for exotics and the study of rare mesons requires measurements of a broad scope of final states in order to consolidate the possible evidence of a resonance by looking at different decay modes and explore poorly-studied reaction channels [? ]. The characteristics of the detector and the trigger conditions foreseen for the experiment - 11 GeV electron beam scattering on a 5 cm long LH<sub>2</sub> target with multiple prongs in the final state - will allow measurements of many final states simultaneously. While the hadrons will be detected in CLAS12, the electron scattered at very small angles and low four-momentum transfer,  $Q^2$ , will be detected in the Forward Tagger (FT), i.e. in the kinematics of quasi-real photoproduction. The FT specifications were thus defined to have the optimal electron detection at low angles

18 compatible with the high rate of electromagnetic background. To reconstruct the quasi-real photon variables  
19 is necessary to measure the scattered electron three momentum. The relevant quantities are:  
20

- 21
- 22 • the energy  $E_{e'}$ : since the photon energy is given  
23 by  $E_\gamma = \nu = E_{\text{Beam}} - E_{e'}$  and its linear polarization by  
24  $P_\gamma = \epsilon^{-1} = 1 + \frac{\nu^2}{2E_{\text{Beam}}E_{e'}}$ ,
  - 25 • the polar angle  $\phi_{e'}$  to determine the polarization  
26 plane,
  - 27 • the azimuthal angle  $\theta_{e'}$ : since  $Q^2 = 4E_{\text{Beam}}E_{e'} \sin^2 \theta/2$ .

28  
29 The Forward Tagger is composed by: an electromagnetic  
30 calorimeter (FT-Cal), to identify the electron, measure  
31 the electromagnetic shower energy and provide a  
32 fast trigger signal, a tracker (FT-Trck), to measure the  
33 scattering angles ( $\theta_{e'}$  and  $\phi_{e'}$ ) with the required accuracy  
34 and a scintillation counter (FT-Hodo) to provide  
35  $e/\gamma$  separation. A dedicated trigger system has been de-  
36 velop to provide a fast signal to trigger the data acquisi-  
37 tion in coincidence with signals from CLAS12.

---

\*Corresponding author  
Email address: marco.battaglieri@ge.infn.it  
(M.Battaglieri)

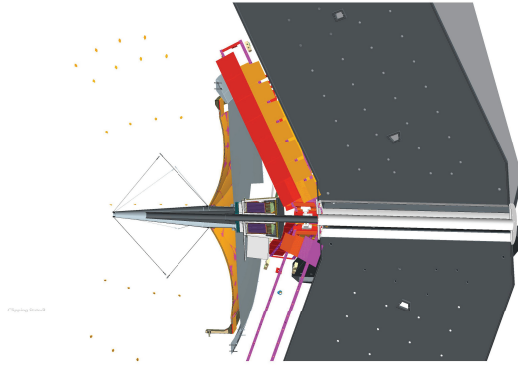


Figure 1: CAD drawing showing the integration of the FT in CLAS12. The FT is located in the free space between the HTCC [?] and the first DC layer [?]. The FT calorimeter shown in blue is located at about 185 cm from the interaction point, shown by the green cross, and is enclosed in a Rohacell case to provide thermal insulation. The scintillation counter (green) and first tracker layer (red) are located in front of the calorimeter. A tungsten cone in black shield the FT from Møller electrons and electromagnetic background created by the beam.

The calorimeter, the scintillation counter and the tracker are placed between the High Threshold Cerenkov Counter (HTCC) and the torus support, at about 185 cm downstream of the target (nominal) position. The close proximity to the beam line ( $2.5^\circ$  corresponds to  $\sim 8$  cm) and the limited space available (at most  $\sim 40$  cm along the beam axis), requires a compact calorimeter with small radiation length and with very good radiation hardness. Figure 1 shows a CAD drawing of the FT integrated in CLAS12. The scintillation counter, placed in front of the calorimeter, is made of plastic scintillator tiles read-out by silicon photomultipliers via wavelength shifting fibers. The tracking detector is then located in front of the scintillation counter to extend the CLAS12 forward tracker down to  $2.5$  degrees. All these components were designed to fit within a  $5.5^\circ$  cone around the beam axis to have no impact on the operation and acceptance of the CLAS12 equipment.

## 2. Detector layout

### 2.1. The EM calorimeter (FT-Cal)

The FT-Cal has to fulfill demanding requirements in terms of: radiation hardness, light yield, shower containment (small radiation length and Moliere radius), fast recovery time, good energy and time resolution.

The electron energy resolution is a crucial factor to determine precisely the photon energy and ensure the

exclusivity of the measured reaction via missing mass technique. However, since we are interested in low energy electrons and high energy photons, the energy resolution on the latter is significantly better than the resolution on the electron<sup>1</sup>. The FT-Cal should have a fast recovery time ( $\tau \sim 10$  ns) to sustain high rates with small pile-up effects and provide the scattered electron interaction time with good accuracy ( $<1$  ns) in order to reject background and identify the signal via coincidence with CLAS12. Due to the expected high rate from electromagnetic background, the calorimeter should be highly segmented in the transverse direction. The size of each pixel should be comparable with the characteristic transverse size of the electromagnetic shower (Moliere radius) to contain the shower produced by incident electrons to few pixels, thus minimizing the pixel rates and pile-up. Finally, the photodetectors for the light readout should work in a sizable magnetic field and has to be small in size to fit within the available space. Thus, the standard photomultipliers can not be used while photodetectors based on semiconductors, e.g. Avalanche Photo Diode (APD), have been shown to meet the required criteria.

To match the necessary requirements, PbWO<sub>4</sub> was chosen as scintillating material and *Large-Area APDs* (LAAPD) as readout sensors. A similar combination was used in CMS-ECal [?], CLAS-IC [?] and PANDA-EMC [?]. Lead-tungstate has a fast scintillation decay time (6.5 ns), a small radiation length (0.9 cm) and small Moliere radius (2.1 cm). The drawback of limited light emission (about 0.3% of NaI(Tl)) has been mitigated by using cooled PbWO Type-II crystals (as PANDA-ECAL) matched to large area photo sensors obtaining a x4 more light per MeV than the original CMS ECal crystals.

With this design an energy resolution of  $(2\%/\sqrt{E(\text{GeV})} \oplus 1\%)$  is expected. Other crystals as LSO/LYSO (or the very recent LaBr) share almost all the good specifications of the PbWO<sub>4</sub> with a light yield more than 100 times bigger. However, the lack of extensive studies on radiation hardness and limited experience in the manufacturing procedures prevented them to be considered as an alternative.

Figure 2:

---

<sup>1</sup>For example, an electron energy resolution of 2% (at 1 GeV) would result in an energy resolution of  $\sim 0.2\%$  for the corresponding 10 GeV photon allowing the use the missing mass technique for the most part of the reactions of interest.

108    2.1.1. *Geometry and coverage*

109    The FT-Cal is made by 332 15x15x200 cm<sup>3</sup> parallel  
 110    lelepiped PbWO<sub>4</sub> Type-II crystals arranged around the  
 111    beam line with full azimuth angular coverage ( $0^\circ < \phi <$   
 112     $360^\circ$ ) and small forward angles acceptance ( $2^\circ < \theta <$   
 113     $5^\circ$ ). Crystals are placed with the long side parallel to  
 114    the beam line to form a ring. Figure 2 shows the crystal  
 115    assembly.

116    2.1.2. *PbWO<sub>4</sub> crystals*

117    FT-Cal PbWO<sub>4</sub> Type-II crystals were produced by  
 118    the Shanghai Institute of Ceramics, Chinese Academy  
 119    (SICCAS). Since the light yield (LY) increases while  
 120    lowering the temperature T according to  $dLY/dT \sim$   
 121     $3\%/\text{ }^\circ\text{C}$ , the calorimeter is stabilized in temperature and  
 122    operated at  $T \sim 0\text{ }^\circ\text{C}$ . Lower T were not considered due  
 123    to a significant complication in the mechanical/thermal  
 124    design, the reduced resistance to radiation and the decay  
 125    time degradation showed by cooled PbWO<sub>4</sub>. The length  
 126    of the crystal (20 cm corresponding to  $\sim 22$  EM radia-  
 127    tion lengths) was chosen to minimize the longitudinal  
 128    loss matching the available clearance.

129    The face lateral size of 15mm x 15mm provides the  
 130    highest pixelization in the transverse plane being of  
 131    the same size of PbWO<sub>4</sub> Moliere radius. All crystals  
 132    were characterized using the ACCOS (Automatic Crys-  
 133    tal quality Control System) facility at CERN [? ]. Ge-  
 134   ometrical dimensions as well as optical properties such  
 135    as longitudinal and transverse transmission and relative  
 136    light yield were determined for each crystals. Samples  
 137    out of the required specifications were rejected and re-  
 138    placed by the manufacturer.

139    The absolute LY (number of detected photo-electron  
 140    per MeV deposited) was found to be  $N_{pe} = 220 \pm 20$  at  
 141     $T = 0\text{ }^\circ\text{C} \pm 0.5\text{ }^\circ\text{C}$ . For this measurement the crystal was  
 142    wrapped on 5 faces with 3M Vikuiti reflective film [? ]  
 143    and light read by a Large Area APD Hamamatsu S8664-  
 144    1010 operated at a G=150 connected with optical grease  
 145    on the free side.

146    The scintillation decay time is also sensitive to the  
 147    temperature. The time constant was measured using the  
 148    *Start-Stop* or *delayed coincidence* method at different  
 149    T. As expected an increase in the decay constant was  
 150    observed by decreasing the temperature. At  $T = 0\text{ }^\circ\text{C} \pm$   
 151     $0.5\text{ }^\circ\text{C}$  we found  $\tau = 13.5 \pm 0.6$  ns ( $\tau_1 = 11.6 \pm 0.5$  ns and  
 152     $\tau_1 = 13.0 \pm 0.2$  ns) when a single (double) exponential  
 153    form was used to fit the data.

154    The radiation hardness of the crystals was measured  
 155    by irradiating crystals with a dose of 30 Gy of low en-  
 156    ergy photons using a <sup>60</sup>Co source at the Strahlenzen-  
 157    trum of Giessen University [? ]. The longitudinal trans-  
 158    mission was measured before and after the irradiation

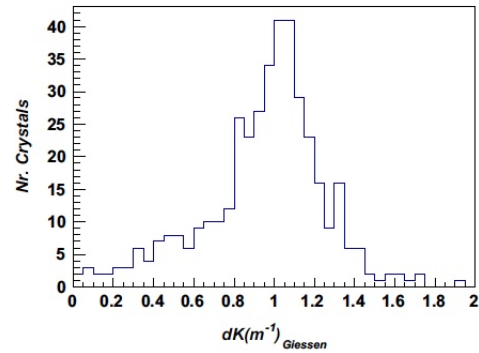


Figure 3: Histogram of the radiation induced absorption coefficient,  $dk$ , for all SICCAS FT-Cal PbWO<sub>4</sub> crystals.

159    calculating the variation as a function of the light-wave  
 160    length. Radiation hardness of the crystals is quantified  
 161    by the radiation induced absorption coefficient defined  
 162    as:

$$163 \quad dk = \frac{1}{\text{length}} \frac{T_{bef}}{T_{irr}} \quad (1)$$

164    where  $T_{bef}$  is the light transmission at 420 nm, the  
 165    peak of the PbWO<sub>4</sub> emission spectrum, measured be-  
 166    fore irradiation, and  $T_{irr}$  the light transmission at the  
 167    same wave-length after irradiation. Crystals exhibiting  
 168    greater levels of radiation damage to light transmission  
 169    have higher values of  $dk$ . All 332 crystals assembled  
 170    in the FT-Cal were individually characterized: on av-  
 171    erage we found  $T_{bef}(420\text{nm}) = 61.5 \pm 0.2$  ( $\sigma = 3.2$ )  
 172    and  $T_{irr}(420\text{nm}) = 50.8 \pm 0.5$  ( $\sigma = 4.9$ ). The resulting  
 173     $dk$  distribution is shown in Fig. 3. These measurements  
 174    were used to optimize the position of each crystal in  
 175    the calorimeter, placing the crystals with the highest ra-  
 176    diation resistance and therefore lowest  $dk$  in the areas  
 177    where the highest radiation dose is expected.

178    2.1.3. *Light readout and electronics*

179    The FT-Cal uses 10x10 mm<sup>2</sup> (model Hamamatsu  
 180    S8664-1010) Large Area Avalanche Photo Diodes  
 181    (LAAPDs) to read out the scintillation light. APDs are  
 182    very compact devices (only few mm thick), have a large  
 183    quantum efficiency at the PbWO<sub>4</sub> light peak emission  
 184    (420 nm), and are insensitive to magnetic fields. The  
 185    main disadvantage is that, due to the low intrinsic gain  
 186    ( $\sim 50 - 200$ ), the output signal is too small to be directly  
 187    acquired, and needs to be amplified by a suitable circuit.  
 188    APDs also need to be operated at controlled tempera-  
 189    ture to avoid variations in gain and noise but this does  
 190    not represent a major complication since the crystals  
 191    too require to be stabilized in temperature. Each sensor

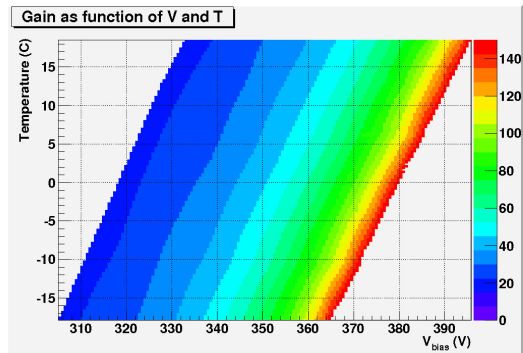


Figure 4: Intrinsic gain of one APD as a function of the bias voltage and of the temperature.

used in the FT-Cal has been characterized by measuring the gain as a function of the applied bias voltage at a given temperature using an automated custom facility (see Ref. [? ] for more details). The typical behaviour  $G(V_{Bias}, T)$  is shown in Fig. 4. The working point (bias voltage) was chosen in order to have the chosen gain ( $G=150$ ) still laying in a reasonably stable region for small variation of the biasing. SiPM readout was not considered due to their limited dynamical range not suitable for spectroscopic application and the limited experience (in term of reliability, radiation hardness, stability in time, ...) in their use in large experiments at the time.

The APD current signal is converted to a voltage pulse which is transmitted to the subsequent electronics chain via a trans-impedance amplifier (i.e. an amplifier which converts an input current pulse into an output voltage pulse, without performing any time integration). This amplifier has been developed in collaboration with the “Service d’Electronique Physique” (SEP) of the “Institut de Physique Nucléaire” (IPN) in Orsay. The amplifier ENC<sup>2</sup> was measured at the operation temperature ( $T=0^{\circ}$  C, finding  $ENC=(8200\pm100)$  e<sup>-</sup> (rms) for the nominal gain of  $G=1800$  (CORRECT TO ACCOUNT THE FINAL GAIN WAS SET TO 600). The amplified signal is read using the custom JLab fADC 250 board (a 16ch, 12 bit, 250 MHz, VME digitizer extensively used at JLab). The measurement of the full wave form allows to derive both charge and time of the hit with the required accuracy.

<sup>2</sup>The ENC, “equivalent noise charge” is defined as the charge transported by that input signal giving, at the output of the amplifier, a signal whose amplitude is equal to the RMS of the output noise.

#### 2.1.4. Light Monitoring System

Lead tungstate scintillating crystals are known as an appropriate material for use in total absorption shower detectors. Unfortunately, although relatively radiation tolerant, they do lower their light output when exposed to radiation and recover when the radiation source is removed. Further complications arise because at the same irradiation intensity, changes in light output may vary from one crystal to another. In order to maintain the intrinsic energy resolution, crystals have to be continuously monitored and if necessary, re-calibrated changing the supply voltage. The monitoring system should be able to test over the time the response of the whole chain: crystal, APD, red-out electronics. Among the different possible options (radioactive source, laser and LED) we used an LED base Light Monitoring System (LMS). In spite of the need of a thermal control, LEDs offer considerable advantages: matching with crystals is more simple than for lasers, since each crystal can have a LED in front of it and the arrangement of electric wires is less critical than optical fibers. The main disadvantage is related to the complexity of the electric circuitry: to cover a large light range keeping a good timing, each LED needs a separate driver leading, for calorimeter of significant size, to a large number of electronic circuits. With LEDs it is possible to obtain a shape and a duration of the monitoring-light flash that would be similar to the features of the crystal scintillation. In fact: the emission spectrum of the monitoring light can be chosen similar to the radio-luminescence spectrum of PbWO<sub>4</sub>, the effective optical path length for monitoring light in the crystal can be matched to the average path length of the scintillation light produced by an electromagnetic shower, and pulse length can be tuned to reproduce the PbWO<sub>4</sub> scintillation decay time. We chose a blue light LED with wavelength close to the 430 nm emission peak of the PbWO<sub>4</sub> crystal and where the radiation damage may have the maximum effect. Each crystal is equipped with a separate LED, located on the upstream face of each crystal, at the opposite end respect to the light sensors and electronics. Intensity can be varied in a range from 500 to 100.000 photons, pulsed at variable rate between 62 Hz to 8 kHz, with pulse rise time of  $\sim 1$  ns and a time jitter less than 200 ps. The system has been designed to work in the temperature range  $-25^{\circ}\text{C} +30^{\circ}\text{C}$ . LEDs, placed in the closed environment of the crystal, is kept at constant temperature with an accuracy of  $\Delta T = 0.1^{\circ}\text{C}$ . The LED monitoring system is split in two boards: one containing the control logic and the LED driver circuits, and the other, to be mounted in front of the FT-Cal crystals, hosting the LEDs. The two

boards are connected via a board-to-board connector allowing the required flexibility to match the FT-Cal geometry and positioning. The LED drivers are controlled by an on-board PIC32 micro-controller accessible remotely via Ethernet. Each LED is individually lighted

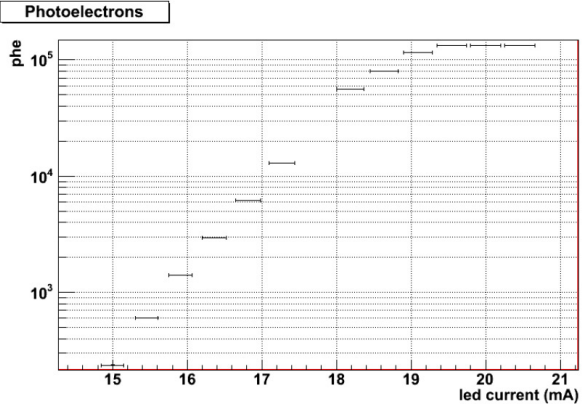


Figure 5: Number of photoelectrons as a function of the driver current. The corresponding energy per crystals range form 10 MeV to 10 GeV.

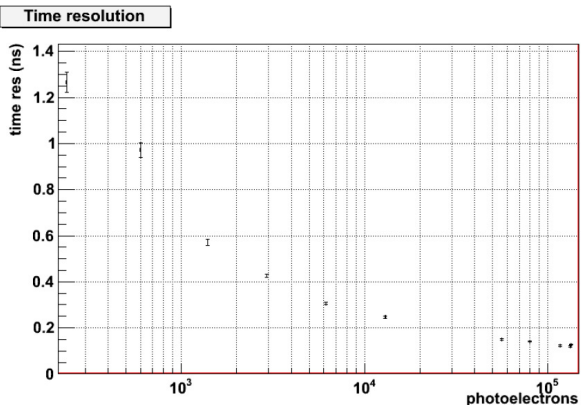


Figure 6: Time resolution measured as the difference of trigger signal and the PMT pulse.

by a programmable lenght and intensity pulse. The system is triggered by an internal clock or by an external signal. In both cases the trigger signal is available for a precise time reference. The performance of the LED driver has been measured coupling a single monitoring channel to a photomultiplier. Performance of the system are reported in Figs. 5 and 6 where the measured photoelectrons as a function of the led current and the measured time resolution as a function of the number of photoelectron are shown<sup>3</sup>. Rescaling results to take into

account the APD readout and the crystal LY/MeV the equivalent energy ranges from 10 MeV (500 phe) to 10 GeV (500k phe) perfectly matched to the expected energy collected by each crystal. A time resolution of 100 ps is reached at high light intensity. Long term stability of the system has been measured and over 100h (4 days) run at T=+18 °C, a stability of each individual channel has been found to be in the range of 2%; when the ratio of the two channels is considered, the stability is at level of few .

### 2.1.5. Slow controls

The FT-Cal slow controls are part of the CLAS12 EPICS system (see Sec. ??). APD needs to be reverse-biased with an high-voltage positive power source. The APD intrinsic gain depends on the bias voltage with  $\frac{1}{G} \frac{\Delta G}{\Delta V} \sim 4\%$  and therefore the power supply needs to be stable in time, with low output noise. We chose the CAEN board A1520P designed for the CMS electromagnetic calorimeter. The power supply fulfills all our requirements in terms of dynamic range, linearity and noise. Each board is equipped with 12 independent channels each of them controlling a group of ten APDs with relative gain variations not greater than 3%.

The amplifiers used in the FT-Cal need to be operated with +5 V and -5 V. The power consumption from each of the two voltage sources is approximately 70 mW, almost independent on the event rate, giving a power consumption of ~140 mW per board, for a total of 56 W for a 400-channels calorimeter. The full FT-Cal is powered by a Wiener *MPOD universal low voltage power supply* MPV8008L, the same module used for other CLAS12 low voltages. Sensing is implemented to compensate the voltage drop across the connecting cables.

Temperature regulation is provided by a Lauda XT150 chiller unit. This is a self regulating unit and does not require external feedback; however the settings and monitored parameters are sent to EPICS for recording via a *streamDevice* module. The FT-Cal temperature is monitored by a set of PT100 thermoresistors, read by a *cRio* module which is being used in the other CLAS12 subsystems, which is part of the interlock system ??.

### 2.1.6. Mechanical design

The mechanical design of the calorimeter is driven by three considerations: minimization of the empty spaces between crystals, cooling to 0 °C; optimal coverage of the requested acceptance without interference with the rest of CLAS12.

The building block of the calorimeter is the single lead-tungstate crystal. Each crystal is 15x15x200 mm<sup>3</sup>, for a weight of 370 g. Each crystal is optically coupled

<sup>3</sup>Time resolution is defined as the sigma of the time difference distribution between the trigger signal and the PMT output.

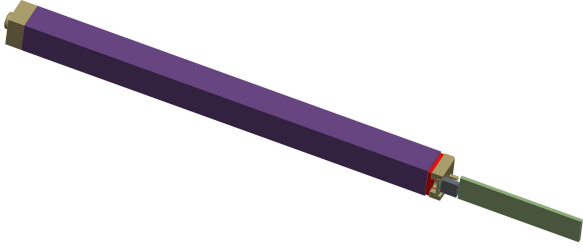


Figure 7: Single crystal assembly: from the left (front) to the right (back), the PEEK holding nose with the LED housing, the crystal wrapped in 3M Vikuiti reflective film, the LAAPD in the PEEK housing, and the preamplifier.

to a Large Area APD on back side and to an LMS LED on the front side for calibration. To achieve the maximum light collection efficiency, the APD covers almost the whole area of the downstream end of the crystal, so the LED for monitoring will be hosted on the upstream end. This reflects onto the mechanical design of the single crystal assembly as a monolithic self-supporting element made of the crystal itself, the APD, the reflective coating and some support structure. To avoid dead volume in the detector, the mechanical support for each crystal is provided only by wrapping. We chose 3M Vikuiti reflective film. This material is non conductive, has a reflectivity higher than aluminized Mylar and, if properly hot-formed, can hold the weight of a crystal. The reflective film is glued on the sides of a pair of front/back PEEK custom-machines blocks that hold the LAAPD and the LED, respectively. Figure 7 shows the CAD rendering of the single crystal assembly from the frontal PEEK support to the preamplifier.

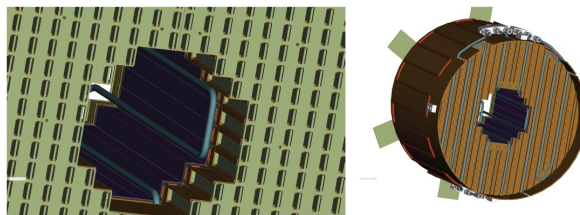


Figure 8: The copper thermal/grounding shield with the cooling pipes.

The crystal assemblies are installed in an matrix to provide complete shower containment for electrons in the FT-Cal angular acceptance. Two copper plates, placed in front and on the back of the crystals, provides load path and positioning for the crystal assemblies. On the APDs side, the preamplifiers, one for each crystal, are connected to the mother board PCB, which is designed to provide power supply, HV distribution and signal collection for each channel. The mechani-

cal structure allows one to replace individual preamplifiers if needed. The front and back copper plates are connected by a copper cylindrical calendar on the outside and by an inner copper shield to form a closed vessel surrounding the crystal matrix to provide proper grounding and the required thermal stability and uniformity. Cooling is provided by 5-mm diameter copper pipes installed on the outside of the vessel as shown by Fig 8. A CAD section view of the complete calorimeter is shown in Fig 9.

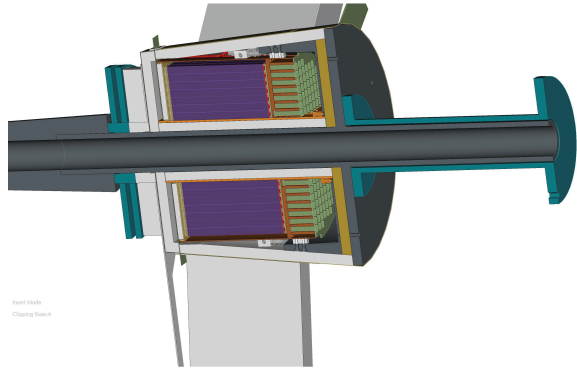


Figure 9: Cross section of the FT calorimeter: in purple, the crystals, upstream the PEEK forward blocks and the forward copper plate, downstream the rear copper plate, the preamplifiers (in green) and the mother board (in white), in light blue and yellow, part of the insulation.

The FT calorimeter has been designed to operate between 0°C to room temperature. FT-Cal cooling is achieved via circulation of coolant in the circuit attached to the rear copper plate and on the inner and outer copper vessels. The cooling system has been designed to compensate the heat inlet coming from the outside world, taking into account 20 mm of insulating foam (Polyisocyanurate, declared thermal conductivity 0:024W/mK) and from the amplifiers, which dissipate ~50 W. The insulation is less effective between the calorimeter and the inner tungsten pipe that holds the entire FT (see Sec. 3), because of the limited space for the insulation and the presence of support structures that bring the overall thermal conductance in that region to 0.056W/mK.

During the design phase, Finite Elements calculation were performed to optimize the cooling circuit and insulation parameters in order to reach the design temperature and uniformity. These studies indicated that the coldest part of the external calorimeter enclosure is the tungsten cone that is expected to stabilize at a temperature just above than the dew point. Measurements per-

399 formed after the calorimeter assembly confirmed these  
 400 results.

#### 401 2.2. The hodoscope (FT-Hodo)

402 The primary aim of the FT-Hodo is to discriminate  
 403 between photons and electrons that produce the electro-  
 404 magnetic shower in the calorimeter. Specifically, elec-  
 405 trons are identified by hits in the hodoscope array which  
 406 are correlated in both position and time with a cluster  
 407 observed in the calorimeter. The FT-Hodo comprises  
 408 an array of 232 plastic scintillator (Eljen-204) tiles seg-  
 409 mented in two layers to suppress contributions from the  
 410 splash-back of the electromagnetic shower created by  
 411 events depositing energy in the FT-Cal. The scintillators  
 412 provide fast timing and sufficient resistance to radiation  
 413 damage for use in the high rate and high dose environ-  
 414 ment of the Forward Tagger. The geometry and read-  
 415 out of the hodoscope are constrained by the surround-  
 416 ing apparatus. Specifically, the device is positioned up-  
 417 stream of the FT-Cal fitting into a circular disk of diam-  
 418 eter 330 mm and 42 mm depth. The readout is achieved  
 419 using  $3 \times 3 \text{ mm}^2$  Hamamatsu S13360-3075PE SiPMs  
 420 (50% photon detection efficiency for 450 nm photons)  
 421 coupled to 5 m long clear optical fibres (Kuraray clear-  
 422 PSM with attenuation length > 10 m), which are fusion  
 423 spliced to  $\sim 30 \text{ cm}$  long wavelength shifting (WLS) Ku-  
 424 raray Y11 fibres (attenuation length of > 3.5 m), embed-  
 425 ded in the scintillator tiles. The splicing induces a pho-  
 426 ton loss of less than 2%, where the use of optical fibres  
 427 allows the captured light to be transported with a light  
 428 loss less than  $\sim 40\%$  over the 5 meter path to the SiPM.  
 429 This readout design of the FT-Hodo addresses the need  
 430 to minimise material in the detector acceptance, to op-  
 431 erate in regions of high magnetic fields produced by the  
 432 CLAS12 solenoid and torus magnets, and to tolerate the  
 433 high background radiation environment.

434 Each layer of the FT-Hodo comprises of 44  $15 \times$   
 435  $15 \text{ mm}$  (P15) and 72  $30 \times 30 \text{ mm}$  (P30) scintillators ar-  
 436 ranged as shown in Fig. 10. The upstream and down-  
 437 stream layers utilize 7 mm and 15 mm thick scin-  
 438 tillator tiles, respectively. The upstream (thin) layer is  
 439 employed to reduce photon conversion in the FT-Hodo,  
 440 while the thicker layer provides the signal with the most  
 441 accurate timing information for the event. To increase  
 442 the number of scintillation photons collected from each  
 443 tile, four WLS fibers were embedded in the P30 tiles  
 444 and 2 in the P15 tiles. In addition, the WLS fibers were  
 445 glued with Bocron BC600 glue (CHECK EpoteK 301-2)  
 446 inside diagonal holes that maximizes the path length in  
 447 the scintillator and allows for the tiles to be arranged  
 448 without any dead space between the elements. Each

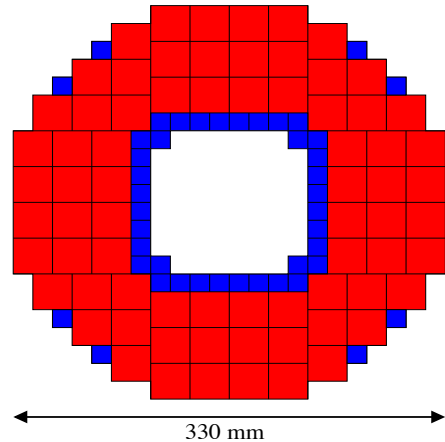


Figure 10: The arrangement of plastic scintillator tiles in the FT-Hodo. The blue (red) squares represent the  $15 \times 15 \text{ mm}$  ( $30 \times 30 \text{ mm}$ ) tiles for each layer.

449 tile was polished and painted with two layers of Bi-  
 450 cron BC620 reflective paint for the sides and 3 layers  
 451 for the scintillator faces and secured in position on the  
 452 surface of a 2 mm thick plastic support board. There  
 453 is a 9 mm clearance for each layer for routing the opti-  
 454 cal fibres to the readout electronics through a  $\Delta$ -shaped  
 455 sheathing on the bottom end of the FT-Hodo. The front  
 456 and back faces are covered by lightproof carbon fiber  
 457 material that is screwed on supporting structures made  
 458 out of hexagonal plastic spacers (15 mm wide and 22 or  
 459 15 mm tall depending on the layer). This results in a  
 460 total detector thickness of 44 mm. A 1 mm thick plas-  
 461 tic strip traces the outer contour of the FT-Hodo and is  
 462 glued on the spacer supports. Figure 11 shows a CAD  
 463 drawing of the FT-Hodo showing half of one layer of  
 464 tiles, the location of the plastic supports for the light  
 465 proofing structure and the plastic strip.

466 With the typical maximum doses determined through  
 467 GEANT4 simulations with realistic beam and target pa-  
 468 rameters and without the shielding effects of the Moeller  
 469 cone (see 3, the FT-Hodo will experience a light loss of  
 470 20% in the WLS fibre [? ] after 3.5 years, whereas the  
 471 plastic scintillators will experience a lightloss of 20%  
 472 after 300 years [? ]). Both scintillators and fibers also  
 473 show natural annealing processes, which can effectively  
 474 compensate for the radiation damage [? ].

475 The analog signal from the SiPM is fed directly to  
 476 a custom designed pre-amplifier board designed by the  
 477 INFN-Genova electronics group. The boards host 8 in-  
 478 dependent channels each coupled to a SiPM and are  
 479 mounted in pairs in the slots of a custom crate, mechani-  
 480 cally compatible with the VME standard. The 16 SiPMs

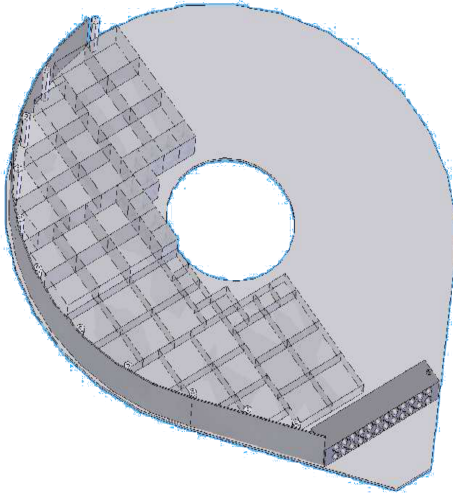


Figure 11: CAD drawing of the FT-Hodo showing half of layer 1, the location of the plastic spacers, and the plastic strip that traces the outer contour.

481 connected to each pair of boards are mounted on a mezzanine PCB, which distribute the bias HV to each SiPM  
482 and collects their signals for the amplifier inputs. The  
483 schematic of one channel of the SiPM amplifier board,  
484 excluding the HV bias network is shown in Fig. 12 The

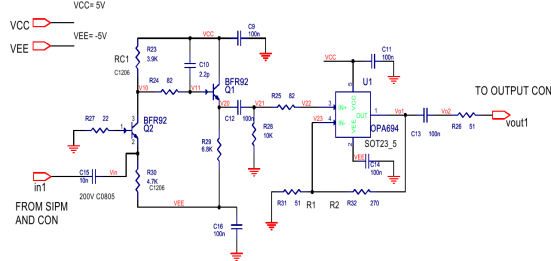


Figure 12: NEED TO Check if UP2Date: Schematic of a single channel of the amplifier board for SiPM.

485 first stage is based on a Bipolar Junction NPN transistor  
486 in a common base configuration, while the second  
487 is composed by a OPA694 operational amplifier in a  
488 non-inverting configuration. The two BRF92 transistors  
489 have been chosen since they are low noise transistors  
490 with a high cut-off frequency and good stability. The  
491 two stages are coupled together with a 100 nF capacitor  
492 to remove the DC component of the signal from the  
493 second transistor. The amplifier is coupled to the output  
494 connector through a 100 nF capacitor and a  $50\ \Omega$  resistor  
495 to remove any DC component from the last stage and  
496 match the impedance of the output cable.  
497

The signal from each SiPM after amplification is con-

499 tinuously digitized by the JLab fADC 250 boards and,  
500 if the trigger condition is satisfied, samples are stored  
501 for further analysis. The data acquisition and slow con-  
502 trols system for the FTHodo are similar to the FTCal  
503 and we refer to that for more details. The SiPMs op-  
504 erate with a bias voltage of 50-55.5 V, which is provided  
505 by three CAEN A1737P HV boards. 30 independent  
506 HV channels are used to operate each SIPM board host-  
507 ing 8 sensors. These groups of 8 SIPMs were selected  
508 according to their gain. The low voltage system used  
509 for the FTHodo is the same as the one used for FTCal.

### 510 2.3. The MicroMegas tracker (FT-Trck)

511 For a precise determination of the scattered elec-  
512 tron angle, a tracker complements the FT-Cal and FT-  
513 Hodo detectors. The FT-Trck uses the same technolo-  
514 gy adopted by the CLAS12 central and forward Mi-  
515 cromegas detectors. We refer to [?] for a detailed  
516 description of these devices. In this section we just de-  
517 scribe the specific design of the FT-Trck.

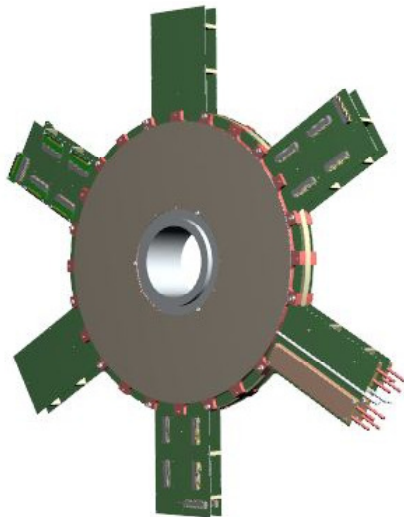


Figure 13: 3D view of the tracker equipped with front-end electronics.

517 Two double-layers of Micromegas detectors are lo-  
518 cated in front of the hodoscope, in the space between the  
519 FT and the High Threshold Cerenkov Counter (HTCC).  
520 Two detectors are indeed a good compromise to achieve  
521 an efficient background rejection and track reconstruc-  
522 tion with a low material budget. Each layer is com-  
523 posed by a double faced Micromegas disk bulked on  
524 a common PCB. Each side of the PCB displays strips,  
525 the downstream ones being perpendicularly oriented to  
526 the upstream ones. This particular geometry enables the

528 determination of the (X,Y) coordinates of a track. To  
 529 limit the number of electronic channels the pitch cho-  
 530 sen was  $500 \mu\text{m}$ , which leads to a resolution better than  
 531 than  $500/\sqrt{12} \sim 150 \mu\text{m}$ . A drift space of 5 mm  
 532 together with an amplification gap of  $128 \mu\text{m}$  provide a  
 533 good efficiency. The two double-layers, centered on the  
 534 beam axes, cover polar angles from  $2.5^\circ$  to  $4.5^\circ$  with  
 535 an active area defined between 70 mm inner radius and  
 536 a 143 mm outer radius. The total number of channel  
 537 is 3072. Figure 13 shows the CAD implementation of  
 538 the detector. the FT-Trck readout uses the same DAQ  
 539 scheme adopted for the CLAS12 Central Micromegas.  
 540 It consists of a Front-End (FE) and a Back-End (BE)  
 541 unit.

542 The FE electronic is responsible for signal pre-  
 543 amplification, shaping, buffering during the trigger gen-  
 544 eration process, data digitization and compression. Due  
 545 to the limited space available, the FE electronic is de-  
 546 signed to be placed off-detector. The micro-coaxial ca-  
 547 ble assemblies connect the detectors and the FE boards.  
 548 Non-amplified analog signals transit via the cable as-  
 549 semblies from the chambers to the FE electronics. The  
 550 512-channel FE Units (FEU) are housed in 4U crates at-  
 551 tached to the FT-Cal mechanical supports and located in  
 552 the shadow of the CLAS12 torus coils.

553 The BE electronic is responsible for data concentra-  
 554 tion providing the interface to CLAS12 event building  
 555 system. It is the same used for the Central Micromegas.  
 556 Details are available in Ref. [?].

557 Each Micromegas layer is powered with 450 V for  
 558 the micro-mesh, and 1000 V for the drift electrode. The  
 559 FT-Trck FE power supply is located 12 m away from the  
 560 crates. The 15 W power produced by each crate is dissi-  
 561 pated by compressed air. An interlock system between  
 562 the cooling infrastructure and the low voltage power  
 563 supply prevents powering the FE crates when cooling is  
 564 off.

565 The gas used is a mixture of Argon, isobutane (up to  
 566 10%) and CF4 (up to 5%). The use of CF4 ensures a  
 567 good time resolution (around 10-15 ns). The gas distri-  
 568 bution is the same of the one used by the Central Mi-  
 569 cromegas system.

### 570 3. Integration in CLAS12

571 The FT mechanical design has been driven by geo-  
 572 metrical constraints imposed by the rest of CLAS12,  
 573 geometrical acceptance optimization and performance  
 574 optimization, taking into account cooling, material bud-  
 575 get, and front-end electronics location. The FT detects  
 576 electrons scattered between  $2.5^\circ$  and  $4.5^\circ$  w.r.t. the beam  
 577 axis. To provide this acceptance, the FT calorimeter

578 must cover down to  $2^\circ$  and up to  $5^\circ$  with lead tungstate  
 579 crystals to have a good containment of E.M. showers at  
 580 the edges of the polar angular range. Since no massive  
 581 materials are allowed at angles larger than  $5.5^\circ$ , crys-  
 582 tals, cooling, mechanical supports and tungsten shield-  
 583 ing have been optimized in a very compact design. Out-  
 584 side this  $5.5^\circ$  we will only have insulating material,  
 585 which has a very low density,  $35 \text{ kg/m}^3$ , and routing for  
 586 cabling and services in the blind area of the CLAS12  
 587 detector, where the torus magnet coils are.

588 The FT is built by several parts that can be grouped  
 589 as follow:

- 590 • the inner tungsten pipe,
- 591 • the tungsten cone acting as Moeller electrons  
592 shield,
- 593 • the tracker,
- 594 • the hodoscope,
- 595 • the calorimeter,
- 596 • the front-end electronics,
- 597 • cabling and services.

598 From the mechanical point of view, the most chal-  
 599 lenging parts are the integration of the calorimeter, due  
 600 to the weight and fragility of the crystals and the relative  
 601 positioning and alignment of the FT components.

#### 602 3.1. Constraints from other sub-detectors

603 The FT must be centered on the beam line be-  
 604 tween the High Threshold Cherenkov Counter (HTCC)  
 605 and the first layer of Drift Chambers. The HTCC can  
 606 be retracted in the upstream direction to give access to  
 607 the FT. In operating position, it extends up to 1730 mm  
 608 downstream w.r.t. the Interaction Point (IP). This plane  
 609 defines the upstream edge of the allowance for the FT.  
 610 The first layer of Drift Chambers is installed in front  
 611 of the toroidal magnet coils, with an inclination of  $65^\circ$   
 612 w.r.t. the beam axis. The front-end electronics boards  
 613 of the Drift Chambers define the downstream border of  
 614 the allowance for the FT. The minimum distance of the  
 615 Drift Chambers boards from the beam axis is  $\sim 140 \text{ mm}$   
 616 at 2280 mm downstream w.r.t. the IP. Taking into ac-  
 617 count the outside radius of the FT, including insulation,  
 618 and the inclination of the Drift Chambers, the FT can  
 619 not exceed  $\sim 2150 \text{ mm}$  w.r.t. the IP.

620 The FT needs cabling and services routing, for gases  
 621 and cooling. These services must be connected to the  
 622 outside of CLAS12. All services are installed in the

623 shadow area of the torus magnet coils, i.e. in six slots  
 624 extending radially from the beam line to the periphery.  
 625 Each coil is  $\sim 100$  mm thick, allowing us to host also  
 626 some front-end electronics, which must be close to the  
 627 detectors.

628 The whole FT is attached to the torus magnet cryostat  
 629 by a support structure with flanges on both ends. This  
 630 is needed both for mounting sequence constraints and  
 631 to avoid massive supports in front of the Drift Chambers.  
 632 The support structure consists of two concentric  
 633 stainless-steel pipes connected by adjustment screws to  
 634 allow for precise alignment and positioning of the de-  
 635 tector w.r.t. the beam line and the IP. A third tungsten  
 636 cylinder of smaller diameter is located inside inside the  
 637 steel pipes to provide shielding from beam background.

638 The FT is attached to the support structure via the  
 639 inner tungsten pipe that is part of the calorimeter assembly  
 640 and is located inside the central holes of the FT detec-  
 641 tors. This pipe is designed to hold the entire weight  
 642 of the FT detectors and of the additional shielding that  
 643 is mounted upstream of the FT. Tungsten was chosen  
 644 as material because, even if less resilient, is more rigid  
 645 than stainless steel reducing the gravitational sagging.  
 646 The FT-Cal is kept in position w.r.t. the inner tung-  
 647 sten pipe via four radial supports, made of PEEK. PEEK  
 648 has been chosen because of its low thermal conductiv-  
 649 ity ( $0.25$  W/m·K) and its relatively high tensile strength  
 650 ( $\sim 100$  MPa). In addition, it features high radiation  
 651 hardness and excellent stability over a broad range of  
 652 temperatures. Mounting rings in peek and aluminum,  
 653 respectively, are used to support and align the FT-Hodo  
 654 and FT-Trk on the inner tungsten pipe.

655 Upstream of the FT, a tungsten cone is attached to  
 656 the inner tungsten pipe to provide shielding from Moller  
 657 electrons produced by the interaction of the beam in the  
 658 target [? ]. Fig. 14 shows a section of CLAS12 with the  
 659 FT in the operating position.

### 660 3.2. Cabling and services routing

661 All services and cables necessary for the operation of  
 662 the FT detectors are routed along the torus coils to mini-  
 663 mize the interference with the CLAS12 Forward Detec-  
 664 tor. These include the following items:

- 665 • FT-Cal:

- 666 1. signal cables (332 coaxial cables with dia-  
 667 meter of 2 mm),
- 668 2. HV (4 multiwire cables with diameter of 10  
 669 mm) and LV cables (1 multiwire cable with  
 670 diameter of 12 mm),

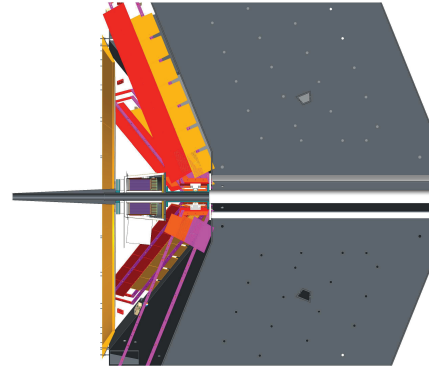


Figure 14: Forward Tagger installed in CLAS12: on the left, the Cherenkov counter, on the right the toroidal magnet cryostat and one sector of the Drift Chambers. Two boxes for front-end electronics, placed in the cryostat shadow, are shown as well.

- 671 3. monitoring and slow controls (1 multiwire  
 672 cable with 14 mm diameter for the readout  
 673 of the temperature sensors and 6 ethernet ca-  
 674 ble for the operation of the light monitoring  
 675 system),
- 676 4. cooling pipes (2 thermally-insulated pipes  
 677 with diameter of 35 mm) and gas lines for  
 678 the nitrogen purge (2 pipes with diameter of  
 679 8 mm);

- 680 • FT-Hodo:

- 681 1. optical fibers (768 1-mm fibers grouped in 48  
 682 bundles for a total diameter of 55 mm);

- 683 • FT-Trk:

- 684 1. optical fibers for the transmission of the dig-  
 685 itized signals (6 fibers with diameter of 2  
 686 mm),
- 687 2. slow controls (3 usb cables),
- 688 3. HV (8 cables) and LV (6 wires with a dia-  
 689 meter of 4 mm) cables,
- 690 4. gas lines (2 pipes with diameter of 12 mm)  
 691 and cooling lines (3 inlet tubes with diameter  
 692 of 35 mm).

693 Cables and pipes are grouped and routed along the di-  
 694 rection of the magnet coils using appropriate rails. The  
 695 rails width and depth has been chosen to be compatible  
 696 with space occupied by CLAS12 Drift Chambers (both  
 697 during normal operation and maintenance) and clear-  
 698 ance between the HTCC and the CLAS12 Forward De-  
 699 tector.

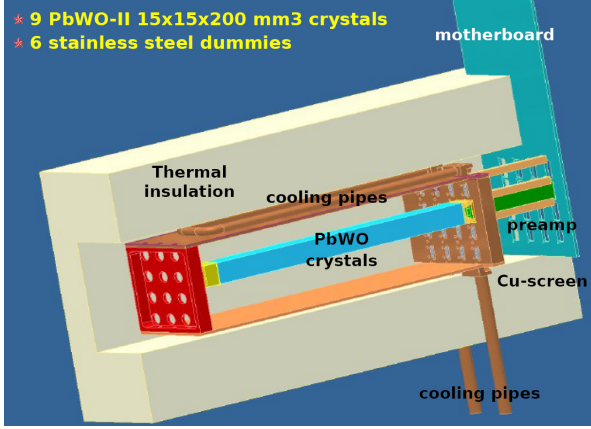


Figure 15: CAD rendering of the FT-Cal Proto-9 assembly. A section of the prototype is shown with a single crystal assembly mounted in the copper shield, which is surrounded by the thermal insulation material. The preamplifier mounted on the right side of the crystal is connected to the motherboard.

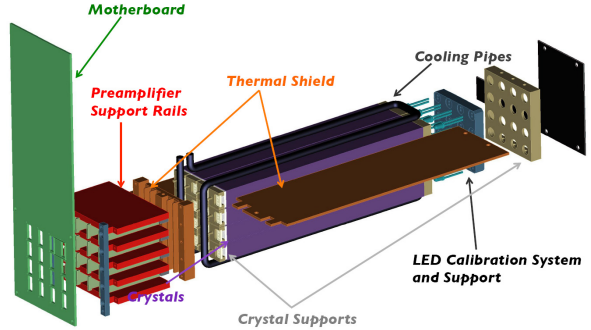


Figure 16: Exploded view of the Proto-16 assembly. From left to right, the CAD drawing shows the motherboard, the system of copper rails holding the preamplifiers, the copper shield back plate, the crystal assembly, the copper shield front plate, the LED board.

- to measure the electronic noise in realistic conditions;
- to perform detailed studies of electromagnetic shower signal: shower profile, APD signal shape, and test of filtering algorithm.

#### 700 4. FT prototypes

701 Two prototypes of the FT-Cal, with 9 and 16 channels  
 702 respectively, were designed, assembled and tested  
 703 with cosmic rays and electron beams to optimize and  
 704 validate the detector design. Specifically, the proto-  
 705 types were used to check the single crystal me-  
 706 chanical assembly, the thermal performance, the front-end  
 707 and read-out electronics, the electrical connections via  
 708 a motherboard. The response to cosmic rays was stud-  
 709 ied for both prototypes while the response to electro-  
 710 magnetic showers was studied at Jefferson Lab and the  
 711 INFN Laboratory Nazionali di Frascati (LNF) in Italy.  
 712 The 9-channels prototype or Proto-9 was tested at JLab  
 713 using 2-3 GeV electrons deflected by the Hall-B tag-  
 714 ger system while the 16-channels prototype or Proto-16  
 715 was tested at the Beam Test Facility of LNF with a 0.5  
 716 GeV electron beam. Extensive simulations have been  
 717 performed and compared to the results of the two sets  
 718 of measurements. Main goals of tests were:

- 719 • to measure the energy resolution as a function of  
 720 single-crystal threshold;
- 721 • to measure the energy resolution as a function of T  
 722 (+18°, 0°, -10°, -25°);
- 723 • to measure the time resolution;
- 724 • to verify the system linearity;
- 725 • to check rate performances;
- 726 • to validate GEMC simulations;

##### 732 4.0.1. The 16-channels prototype

733 The FT-Cal Proto-16 was built assembling 16 crys-  
 734 tals in a 4 × 4 matrix (8 provided by the BTCP and 8  
 735 from the RIINC company). Figure 16 shows the Proto-  
 736 16 components. Many mechanical and electrical solu-  
 737 tions tested on Proto-16 were then adopted in the final  
 738 FT-Cal design. Due to a significant size of the crystal  
 739 matrix the expected performance of Proto-16 in terms  
 740 of energy resolution for showers generated at the center  
 741 of the 4x4 matrix are similar to what expected for the the  
 742 FT-Cal. The Proto-16 was tested at the Beam Test Facil-  
 743 ity (BTF) [1] of LNF, using a 500 MeV electron beam.  
 744 Data were taken in October 2012 studying the prototype  
 745 resolution as a function of the energy and calorimeter  
 746 temperature. The BTF electron beam is characterized  
 747 a repetition frequency of 50 Hz and a pulse duration of  
 748 10 ns. The beam intensity can be varied by operating  
 749 different sets of slits, selecting the number of electrons  
 750 per bunch at the level of a single particle. The prototype  
 751 performance can therefore be studied as a function of  
 752 the number of electrons hitting simultaneously the crys-  
 753 tal matrix, i.e. of the detected energy.

754 Fig. 17 shows the experimental hall after the instal-  
 755 lation of the Proto-16 and associated equipment. The  
 756 detector was placed on a movable table that can be dis-  
 757 placed in the x and y direction with 0.1-mm accuracy.  
 758 This feature was exploited to center the calorimeter with  
 759 respect to the beam. A plastic scintillator bar, read by  
 760 two PMTs, was placed in front of the beam pipe exit



Figure 17: Experimental setup of the Proto-16 test at the LNF Beam Test Facility (BTF).

761 window and was used to determine the arrival time of  
 762 the electron within the 10-ns bunch duration. The data  
 763 acquisition, based on the JLAB DAQ standard CODA,  
 764 was triggered by the RF signal of the Frascati accel-  
 765 erator. For each trigger all the signals of the Proto-  
 766 16 crystal matrix and of the scintillator-bar PMTs were  
 767 recorded by CAEN VME boards. Both the Proto-16 and  
 768 scintillator signals were sent to a passive splitter whose  
 769 two outputs were connected the 250 MHz fADCs and  
 770 to leading-edge discriminators. The discriminator out-  
 771 put was sent to pipeline TDCs. The samples recorded  
 772 by the fADCs in a 800 ns window were recorded for  
 773 each trigger and analyzed offline to evaluate the charge  
 774 and time.

775 The conversion between charge and energy was first  
 776 determined using cosmic ray measurements and then  
 777 optimized by studying the response of each crystal to  
 778 500 MeV electrons at the LNF-BTF. It worth notic-  
 779 ing that the new calibration constants were found to be  
 780 within 5-10% from the initial values determined with  
 781 the cosmic-ray data taking. The total reconstructed en-  
 782 ergy after the full calibration is shown in Fig. 18 for  
 783 an electron multiplicity of the order of 1-2. The peaks  
 784 corresponding to different bunch population are clearly  
 785 visible and well separated.

786 *Energy resolution.* The mean values and  $\sigma$  of the peaks  
 787 in the total reconstructed energy spectrum were ana-  
 788 lyzed to check the system linearity and determine the  
 789 resolution. The measurements were performed by cen-  
 790 tering the beam on the calorimeter to have the maximum  
 791 containment of the electromagnetic shower. Fig. 19  
 792 shows the fitted peak position as a function of total en-  
 793 ergy in the beam bunch for APD gain of 150 and PbWO

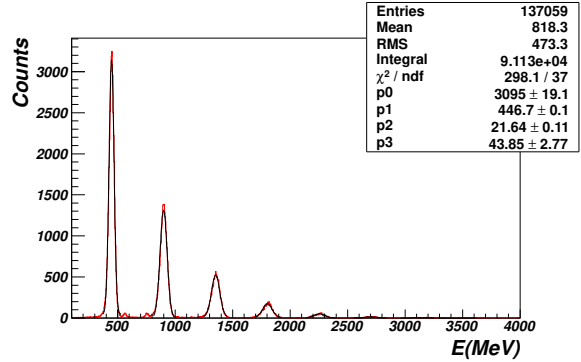


Figure 18: The total energy measured by Proto-16 after calibration. Peaks corresponding to different bunch population are clearly and well separated.

794 temperature of  $18^\circ$ . The linear regression of the ex-  
 795 perimental points show no deviations from linearity in  
 796 the explored range. The same measurement performed  
 797 in different configurations gave consistent results, con-  
 798 firming that the system is linear up to the maximum  
 799 measured energy of 4 GeV.

800 Fig. 20 shows the energy resolution as a function of  
 801 the energy in the beam bunch. The colored points cor-  
 802 respond to the resolution measured with the Proto-16  
 803 while the black open circle are the results of the GEMC  
 804 simulations. The error bars in the graph show the sta-  
 805 tistical uncertainty while the systematic uncertainty was  
 806 estimated to be in the order of 5%. As expected, the  
 807 experimental resolution increases for increasing energy,  
 808 reaching an asymptotic behavior at about 3 GeV. The  
 809 measurements performed in different configuration are  
 810 in general consistent, varying within a range of 0.5% ex-  
 811 cept for the resolution obtained at room temperature and  
 812  $G=75$  (orange points). The resolution in this case is sys-  
 813 tematically worse than what obtained at the same tem-  
 814 perature but  $G=150$ . This was interpreted as due to the  
 815 preamplifier noise being the dominant factor in deter-  
 816 mining the resolution at this temperature. From this we  
 817 concluded that working at high APD gain is the prefer-  
 818 able configuration.

819 The comparison of the resolution obtained at differ-  
 820 ent temperature show that lower temperatures, corre-  
 821 sponding to higher light yield and therefore larger sig-  
 822 nals, give better resolution. The best values were ob-  
 823 tained at  $-20^\circ$ , where the experimental points are in  
 824 good agreement with the simulation results. The de-  
 825 pendence of the resolution on the temperature is more  
 826 evident for high bunch energies, where threshold effects  
 827 are smaller. Above 2 GeV, the resolution at room tem-  
 828 perature seems to be systematically higher than the one

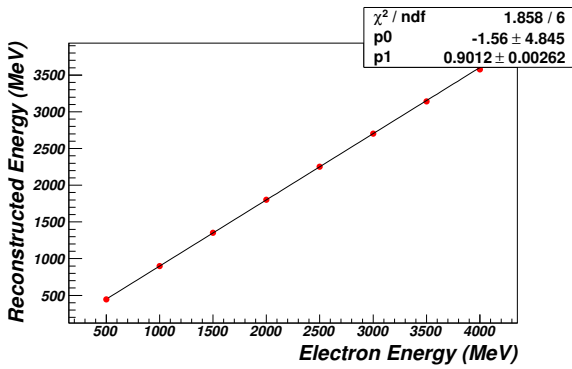


Figure 19: Proto-16 reconstructed energy as a function of the beam bunch energy. The red points were obtained at room temperature and with a APD gain of 150. The linear regression of the experimental points show no deviation from linearity.

829 obtained at  $0^\circ$  or  $-20^\circ$  with a difference of about 0.5%.  
 830 The difference of the resolution obtained at  $0^\circ$  and  $-20^\circ$   
 831 is on the contrary quite small and negligible within the  
 832 systematic errors. Based on this results and considering  
 833 the technical difficulties in operating the FT-Cal at very  
 834 low temperature, we concluded that the optimal operating  
 835 temperature of the calorimeter is  $0^\circ$ .

## 836 5. Detector calibration and commissioning

### 837 5.1. Pre-beam calibration

838 Initial checkout and calibrations of the FT detectors  
 839 upon completion of the installation were performed via:

- 840 • Pulser, LED and cosmic ray runs for the FT-Cal;
- 841 • Pulser and cosmic ray runs for the FT-Hodo;
- 842 • Pulser and pedestal runs for the FT-Trk.

#### 843 5.1.1. FT-Cal pre-beam calibration

844 Initial checkout of the calorimeter is performed via  
 845 pulser and LED runs.

846 In pulser runs, an external clock is used to trigger the  
 847 readout of the entire FT-Cal recording the full fADC  
 848 waveforms in a 400 ns window in the absence of a  
 849 physics signal to measure baselines and monitor noise,  
 850 for the purpose of identifying disconnected or malfunc-  
 851 tioning channels. For each crystal, several parame-  
 852 ters such as the average pedestal, the event-by-event  
 853 pedestal RMS or the noise defined as the sample-by-  
 854 sample pedestal RMS. The analysis can be performed  
 855 online, connecting to the DAQ Event Transfer (ET) ring  
 856 [?], or from a recorded EVIO file using the FT Java cal-  
 857 ibration suite [?]. Figure 21 shows a view of a typical

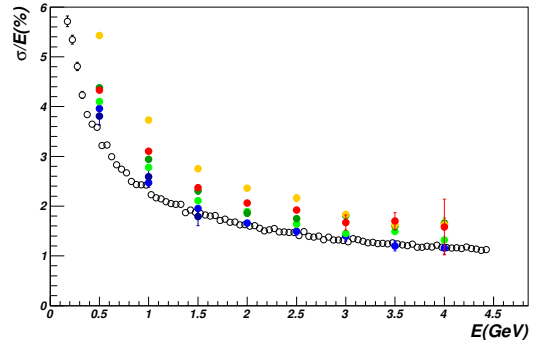


Figure 20: Proto-16 energy resolution as a function of the beam bunch energy. The red and orange points were obtained at room temperature for an APD gain of 150 and 75, respectively. The green points correspond to  $0^\circ$  degrees; the darker points were obtained removing the passive splitter. The blue and dark-blue points correspond to  $-20^\circ$  with APD gain of 150 and 75, respectively. The open black circle show the expected resolution based on GEMC simulations. Only statistical errors are shown.

858 pulser run analysis as displayed by the calibration suite.  
 859 Among the most useful information available from this  
 860 analysis is the channel average noise that is indicative of  
 861 its functionality: a noise level below the typical range is  
 862 indicative of a malfunctioning preamplifier or discon-  
 863 nected cable while a noise level above the the typical  
 864 range can indicate a high-voltage issue since the noise  
 865 introduced by the LAAPDs is higher when the biased  
 866 voltage is not applied.

867 Once the initial debugging of the system is completed  
 868 based on pulser runs, a second checkout is performed  
 869 based on LED runs. In this case, the FT-Cal LMS is  
 870 used to input light in each of the calorimeter crystals  
 871 and the corresponding signals are recorded to check  
 872 the pulse amplitude and shape and assess the correct  
 873 functioning of the LAAPDs, preamplifiers and front-  
 874 end electronics. Using the EPICS slow controls inter-  
 875 face of the LMS, the LEDs are switched on in groups of  
 876 6, one per driver, in a predefined sequence and pulsed at  
 877 a rate of 62.5 Hz for a time interval of 30 s to accumu-  
 878 late about 1800 waveforms per channel. The LED pulse  
 879 amplitudes have been tuned to provide a maximum am-  
 880 plitude at the fADC of about 1 V, which is representa-  
 881 tive of a typical signal expected for the calorimeter. The  
 882 recorded waveforms are analyzed to extract the pulse  
 883 amplitude as a function of time. In fact, upon being  
 884 turned on, the LED light intensity undergoes an expo-  
 885 nential drop until it reaches stability. This happens typi-  
 886 cally within 6-8 s. The amplitude in the stability region  
 887 is fitted to a constant to extract the average value that  
 888 is recorded and compared to reference values to detect

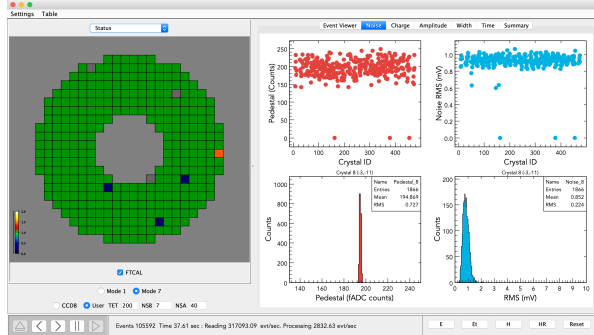


Figure 21: Results of the FTCal noise analysis from a pulser run. The left part of the calibration suite display shows a view of the calorimeter with a color scheme representing the status of the crystal: green corresponds to a fully functional element, blue to an elements with noise below the typical range that is indicative of a low gain preamplifier, orange to an element with noise above the typical range and gray to a crystal for which no data were recorded. The right part of the panel shows the average pedestal and noise as a function of the crystal number, and the event distribution of the pedestal and noise for the selected crystal.

changes in the detector response and potential failures. Fig. 22 shows the results of the analysis of a typical LED run as displayed by the calibration GUI. In the specific case, the analysis shows a relatively uniform response to the LED light, with typical amplitudes of the order of 1 V as defined by design, with few problematic channels that coincides with the ones identified by the pulse runs of Fig. 21.

The final mean of calibration without beam is based on the study of the detector response to cosmic rays. A special FPGA-based trigger was developed by the JLAB Fast Electronic Group to select events where a cosmic ray crosses the calorimeter primarily in the vertical direction, i.e. crossing the crystals along the short side. This is achieved by requesting to have a minimum number of signals above threshold in the crystals that are in a "column" of the calorimeter assembly. This is achieved by exploiting the functionalities of the JLAB fADCs and VTPs [? ?]. For these events, waveforms for all crystals in the calorimeter are recorded and analyzed offline using the FT-Cal calibration suite. Details of the analysis procedure are reported in Refs. [? ?]; here we summarize only the main steps and results. For each crystal, events where at least  $N_{min}$  crystals with signal above thresholds are found in a vertical range of  $N_{range}$  crystals above or below the chosen one. After optimization, the values of  $N_{min}$  and  $N_{range}$  were fixed to 4 and 5, respectively. For these events,

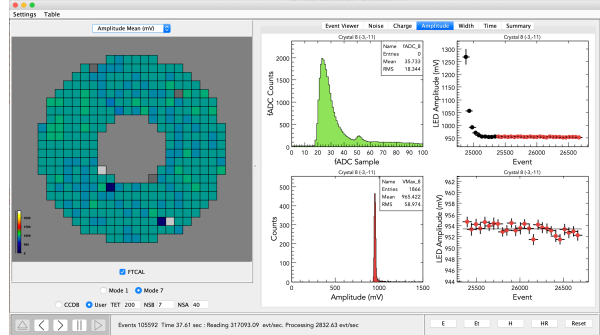


Figure 22: Results of a typical FTCal LED run. The left part of the calibration suite display shows a view of the calorimeter with a color scheme representing the LED pulse amplitude. The right part of the panel shows for the selected crystal the average pulse shape (top left), the pulse amplitude as a function of the event number, i.e. of time (top right), the distribution of the amplitudes (bottom left) and the pulse amplitude as a function event number after the LED has reached stability (bottom right). The latter is fitted to a constant to determine the pulse amplitude that us displayed in the detector view.

the crystal waveform is integrated in a fixed range and pedestal subtracted to extract the charge. The integration range was optimized empirically to maximize the signal to noise ratio compatibly with the signal time jitter with respect to the trigger. The charge distribution for all selected events in the given crystal is then fitted with a Landau summed to an exponential function, representing the minimum ionizing particle deposition and noise, respectively. The mean of the Landau function, compared to the expected average energy deposition estimated to be 15.3 MeV via GEANT4 simulations, is then used to evaluate the charge-to-energy conversion factor for each crystal. Fig. 23 shows an example of a cosmic ray event as displayed by the calibration suite and an example of the charge distribution for a selected crystal obtained by integrating over the selected events. The typical values of the Landau means are found to be in the range of 4-7 pC at the calorimeter operating temperature of 0° C and the corresponding conversion factors in the range of 2.2-3.8 MeV/pC. These values were used as calibration constants for the initial reconstruction of beam data, finding that these usually lead to overestimate by 20% the actual energy deposited in the energy range of interest for the calorimeter, i.e. 0.5-4.5 GeV. While this discrepancy is significant, it is not unexpected given the uncertainties in extracting the cosmic ray signal from the noise and the two order of magnitudes between the cosmic ray calibration point and the energy range for beam induced signals.

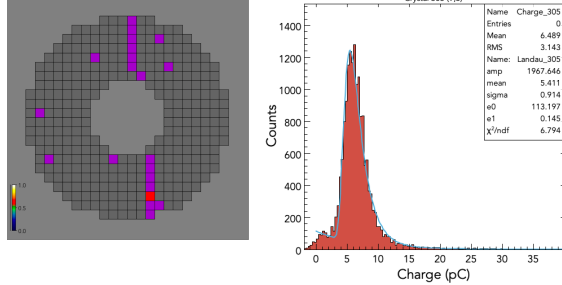


Figure 23: Left: example of a cosmic ray crossing the calorimeter vertically as displayed by the calibrations suite. Right: example of the measured charge distribution measured from the selected events for a calorimeter crystal; the blue line shows the results of the Landau plus exponential fit; the mean of the Landau function is used to estimate the charge-to-energy conversion factors.

#### 946 5.1.2. FT-Hodo pre-beam calibration

947 Similarly to the calorimeter, initial checkout of the  
 948 hodoscope is performed via pulser runs to check the  
 949 functionality of each electronic channel and evaluate  
 950 the SiPM gains by measure the Single Photo-Electron  
 951 (SPE) signal. An external clock is used to trigger the  
 952 data acquisition recording the waveform of all the 232  
 953 channels in a 400 nS windows. The waveforms can be  
 954 analyzed online by connecting the calibration suite to  
 955 the DAQ ET ring or offline reading from file. The  
 956 parameters that are monitored are the pedestal values, the  
 957 pedestal RMS and the electronic noise. The extracted  
 958 values are compared to the typical ones to identify prob-  
 959 lematic channels and disconnected cables. For each  
 960 channel, waveforms that exceed a minimum threshold  
 961 above the baselines are analyzed to extract the SPE sig-  
 962 nal. For this purpose, the waveforms are integrated in  
 963 a fixed time range and pedestal subtracted. The dis-  
 964 tribution of the extracted charge for a selected channel is  
 965 shown in Fig. 24. Clear peaks corresponding to one,  
 966 two and three photo-electrons are visible; the difference  
 967 between two peaks is used to determine the gain of the  
 968 channel finding typical values of the order of 20 pC.

969 Further checkout of the detector is performed via cos-  
 970 mic ray data taking. The same FPGA based trigger de-  
 971 veloped for the calorimeter is used to trigger the DAQ  
 972 on events in which multiple tiles of the hodoscope have  
 973 a signal above threshold. For such events, all hodoscope  
 974 channel waveforms are recorded and analyzed offline.  
 975 The signal charge is extracted integrating the waveform  
 976 in a fixed time window and subtracting the pedestals.  
 977 The resulting charge distributions are inspected to en-  
 978 sure a sizable signal for all tiles. In this case no attempt

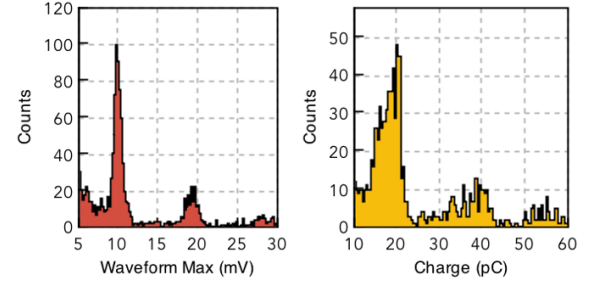


Figure 24: SPE signal from a single Hodoscope SiPM in mV (left) and pC (right) determined using the waveform max and integral re-  
 spectively.

979 is made to extract the charge-to-energy conversion fac-  
 980 tor from these distributions because of the unfavorable  
 981 orientation of the hodoscope in the installation position  
 982 for the measurement of cosmic ray that can cross the  
 983 scintillation tiles with a very large angular spread and  
 984 therefore of path lengths within the active volumes.

#### 985 5.1.3. FT-Trk pre-beam calibration

986 The initial checkout of the FT tracker and in partic-  
 987 ular of the front-end electronics is performed by means  
 988 of pedestal and pulser runs. Since these procedures are  
 989 standard for the CLAS12 MicroMegas detectors, we re-  
 990 fer to Ref. [?] for further details.

### 991 5.2. On-beam calibration and commissioning

992 While pre-beam calibration are essential to ensure all  
 993 detector components are fully operational, the final cal-  
 994ibrations to extract the parameters needed for the FT re-  
 995 construction are based on analysis of beam data. Here  
 996 we report specifically on the procedures developed for  
 997 the calibration of the calorimeter and hodoscope, since  
 998 no specific calibrations are needed for the tracker.

999 For both hodoscope and calorimeter, energy and time  
 1000 calibrations can be obtained from the analysis of data  
 1001 recorded with the CLAS12 production triggers and do  
 1002 not require dedicated data taking. A dedicated run is  
 1003 typically employed, however, for matching the gains  
 1004 from all Hodoscope SiPMs <sup>4</sup>. In this dedicated run, aver-  
 1005 age MIP signals are obtained for a set of different HV  
 1006 settings (see Fig. ??), determining two constants from  
 1007 which gain matching is established.

1008 Energy calibration for the FT-Cal is achieved by an-  
 1009 alyzing electron elastic scattering events or by recon-  
 1010 structing the  $\pi^0 \rightarrow \gamma\gamma$  decay where both photons are  
 1011 detected in the calorimeter.

<sup>4</sup>Having a matched gain from all Hodoscope SiPMs allows having a common VTP threshold for all channels.

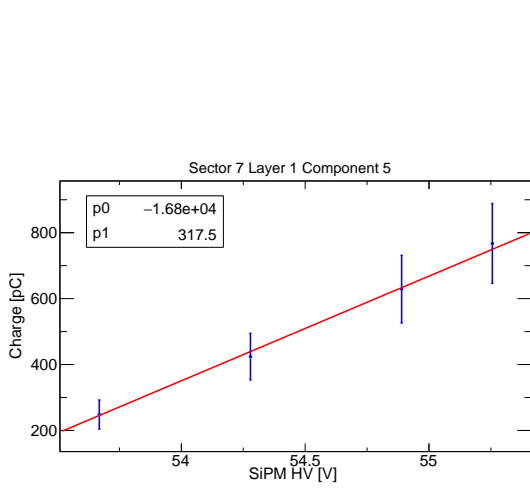


Figure 25: Gain-matching constant determination for a single SiPM.

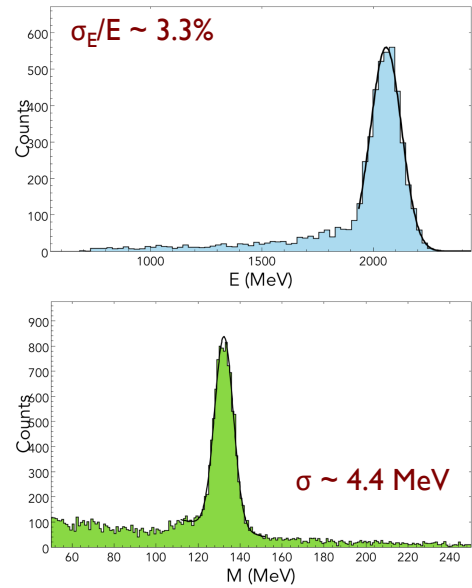


Figure 27: Left: electron energy spectrum reconstructed at 2.2 GeV beam energy in the FT-Cal; the peak corresponds to elastic scattering; after calibrations based on elastic events, an overall energy resolution of 3.3% at 2.2 GeV is found. Right:  $\pi^0 \rightarrow \gamma\gamma$  invariant mass spectrum reconstructed at 10.6 GeV beam energy using the elastic scattering energy calibrations: the width of the  $\pi^0$  peak determined via a Gaussian fit was found to be of  $\sim 4.4$  MeV.

```

1012
1013
1014
1015
1016
1017
1018
1019
1020
1021
1022
1023
1024
1025
1026
1027
1028
1029
1030
1031
1032
1033
1034
1035
1036

```

fig/ftcal\_elasticcal.pdf

Figure 26: aaa

Elastic scattering calibration was found to be particularly effective at low beam energy and was performed using 2.2 GeV beam data recorded during the CLAS12 engineering run. Events with only one cluster in the FT-Cal were selected and, based on the existing cosmic ray calibrations, the energy of the crystal with the largest signal, i.e. the *seed*, was extracted. For crystal, these events were accumulated requesting the seed energy to be larger than 55% of the total cluster energy. The right edge of the distribution of the seed energy was fitted with a Gaussian function to extract the peak position. The mean value of the Gaussian function was compared to what expected based on GEANT4 simulations to extract a correction to the charge-to-energy conversion factor used in the cluster reconstruction. Fig. ?? shows an example of the seed energy distribution and the cluster energy distribution for a selected crystal. Using these constants, an energy resolution of 3.3% at 2.2 GeV beam energy was determined by fitting the reconstructed elastic peak (see Fig. 27). With the same calibration constants, the  $\pi^0 \rightarrow \gamma\gamma$  decay was reconstructed at 10.6 GeV beam energy selecting events with both photons detected in the FT-Cal, finding the width of the  $\pi^0$  peak is of the order of  $\sim 4.4$  MeV.

Since the effectiveness of the elastic calibration is

1037 limited to beam energy of the order of few GeV because  
 1038 of rapid decrease of the corresponding cross section at  
 1039 higher energies, an alternative approach was developed to  
 1040 perform the energy calibration of the FT-Cal based on  
 1041 the  $\pi^0 \rightarrow \gamma\gamma$  decay. Events where both photons are  
 1042 detected in the calorimeter were selected and filtered applying  
 1043 the following cuts:

- 1044 • the energy of both clusters, as reconstructed based  
 1045 on existing calibrations is larger than 500 MeV,  
 1046 • the size of both clusters, i.e. the number of crystals  
 1047 involved, is larger than 3,  
 1048 • the opening angle between the two clusters is  
 1049 larger than  $2^\circ$  deg.

1050 The last cut is useful to reduce background resulting  
 1051 from split clusters. For each crystal, events in which  
 1052 the crystal is the seed of one of the two clusters are  
 1053 accumulated and the ratio between the measured cluster  
 1054 energy for the given crystal and the energy calculated  
 1055 from the nominal  $\pi^0$  mass and the other cluster energy is  
 1056 computed. The distribution of such ratios is  
 1057 fitted with a Gaussian function to derive a correction  
 1058 factor for the charge-to-energy calibration constant of  
 1059 the selected crystal. The procedure is applied iteratively  
 1060 until the  $\pi^0$  mass spectrum for all crystal is within 0.5  
 1061 MeV from the nominal value. Fig. 28 shows an exam-  
 1062 ple of the ratio distribution and of the  $\pi^0$  mass spectrum  
 1063 for a selected crystal before and after (blue histogram)  
 1064 the calibration procedure. The advantage of this pro-  
 1065 cedure is that it does not strongly depends on the beam  
 1066 energy and exploits the full energy spectrum of the  
 1067 clusters providing a check of the linearity. The left panel of  
 1068 Fig. 28 shows the correlation between the measured and  
 1069 computed cluster energies after calibrations: the energy  
 1070 range, which is covered with good statistics, is from 0.5  
 1071 to 5 GeV with a perfect overlap with the energy range of  
 1072 interest for the FT. The resolution that is achieved with  
 1073 this calibration algorithm is of the order of 4-5 MeV in-  
 1074 tegrated on the whole calorimeter as shown by the right  
 1075 panel of Fig. 29.

1076 Energy calibration of the FT-Hodo is performed by  
 1077 studying the energy deposition of minimum ionizing  
 1078 particles. Fig. 30 shows the charge from MIP signals  
 1079 in the thin and thick tiles. For the FT-Hodo, charge par-  
 1080 ticle signals are selected by requiring the geometrical  
 1081 matching of tiles in the two layers. The distribution are  
 1082 fitted with a Landau plus an exponential function to de-  
 1083 termine the average MIP charge. The charge-to-energy  
 1084 conversion factors are determined by comparing the re-  
 1085 sulting values to the ones estimated from GEANT4 sim-  
 1086 ulations.

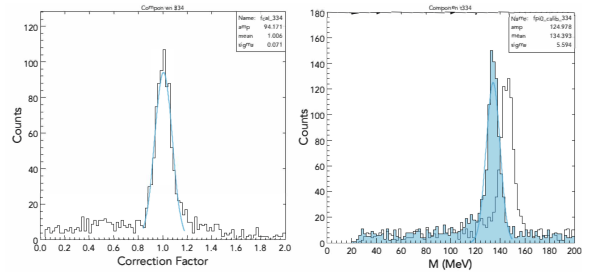


Figure 28: Left: calibration correction factor for a selected crystal computed as the ratio between the measured energy of clusters where the crystal is the seed and the energy calculated from the nominal  $\pi^0$  mass and the other cluster energy. Right:  $\pi^0$  mass spectrum for the same crystal before and after the calibration procedure.

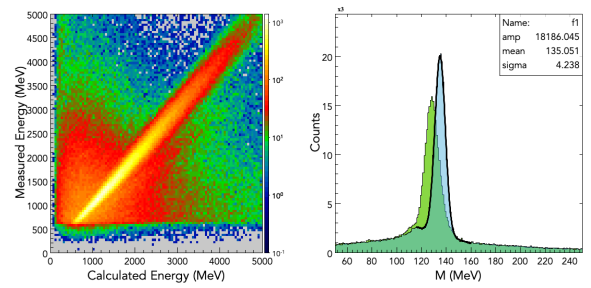


Figure 29: Left: correlation between the measured cluster energy and the energy computed from the nominal  $\pi^0$  mass; the range covered is well matched to the FT energy range of interest. Right:  $\pi^0$  mass spectrum before (green) and after (blue) the calibration; the achieved resolution is of  $\sim 4.2$  MeV.

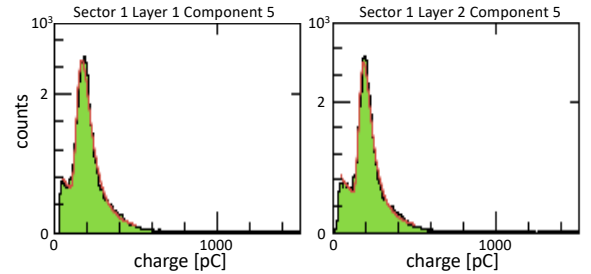


Figure 30: Signal from two Hodoscope tiles (thin and thick layer) fitted with a Landau plus an exponential to establish the charge-to-energy constants.

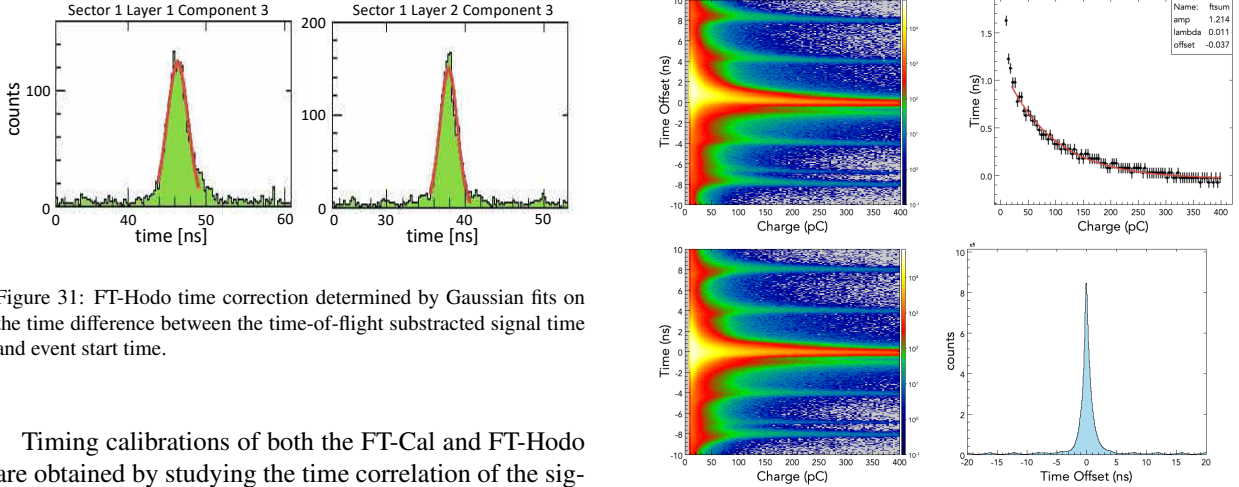


Figure 31: FT-Hodo time correction determined by Gaussian fits on the time difference between the time-of-flight subtracted signal time and event start time.

Timing calibrations of both the FT-Cal and FT-Hodo are obtained by studying the time correlation of the signals detected in the two detectors and the CLAS12 Forward Time-Flight (FTOF) detector [? ]. Events with a scattered electron in the CLAS12 forward detectors and a second particle is detected in the FT are selected. In such events, the start time  $t_0$ , i.e. the time of interaction of the beam electron in the target, can be computed from the electron FTOF time subtracted of the time-of-flight from the vertex to the FTOF. The start time can then be used as a reference for the calibration of the FT detectors.

For the FT-Hodo, the signal time,  $t_{hit}$ , subtracted of the time-of-flight from the vertex to the detector, is compared to the event start time,  $t_0$ . The difference between the two gives the time correction needed. Fig. 31 shows an example of the time offset distribution for a thin and a thick tile.

The same procedure is used for the FT-Cal, for which however all hits with energy greater than 10 MeV are used with no requirements on the charge of the associated particle. The use of such low energy threshold is important to be able to calibrate the crystals that are on the edges of the calorimeter. The measured time is then compared with the event start time, extracting both an overall offset and a charge-dependent correction, associated to a time-walk effect. The top-left panel of figure Fig. 32 shows the time offset as a function of the signal charge; this histogram profile is fitted to a power law,  $a/q^l$ , as shown in the top-right panel to determine the time-walk correction. After applying this correction, the time offset distribution shown in the bottom plots of the same figure are fitted to a simple Gaussian function to determine the global offset. The bottom right is the final distribution with all corrections, showing a clear coincidence peak at 0 surrounded by the accidental peaks at multiple of  $\pm 4.008$  ns due to the RF beam structure. The time offset constant term is extracted for

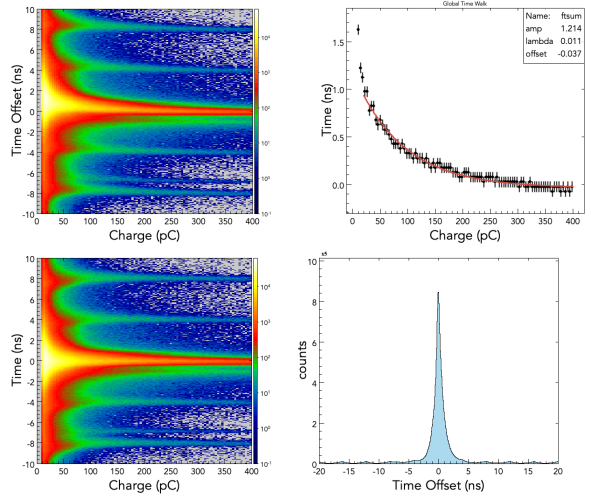


Figure 32: Top: FT-Cal time offset dependence on the charge (left); the profile of the histogram is fitted to a power law,  $a/q^l$ . Bottom: FT-Cal time offsets after the time walk and the subtraction of the residual constant term.

each crystal separately, while the time walk constants are fitted for all crystal together since no significant difference between crystals was found.

## 6. Simulations

Detailed simulations of the FT have been done with the GEANT4-based Monte Carlo code for CLAS12, GEMC [? ] to optimize the detectors design, develop reconstruction algorithms and understand the detectors performance.

Details on the implementation in GEMC of the detector geometry and digitization are reported in Ref. gemc, while an extensive discussion of the simulation studies that guided the detector design are presented in Ref. [? ]. Here we focus on summarizing the results of simulations studies that are relevant to understand the FT performance.

### 6.0.1. Leakage corrections

The reconstructed cluster energy can result to be systematically smaller than the actual energy of the particle that induced the shower. This is due to leakages in the shower containment caused by the limited dimension of the calorimeter, by cuts in the clustering algorithms and thresholds in the hit detection. An example of the difference between the reconstructed cluster energy and the simulated electron energy is shown in the top panel of Fig. 33. This was obtained assuming an equivalent threshold on the individual crystals of 10

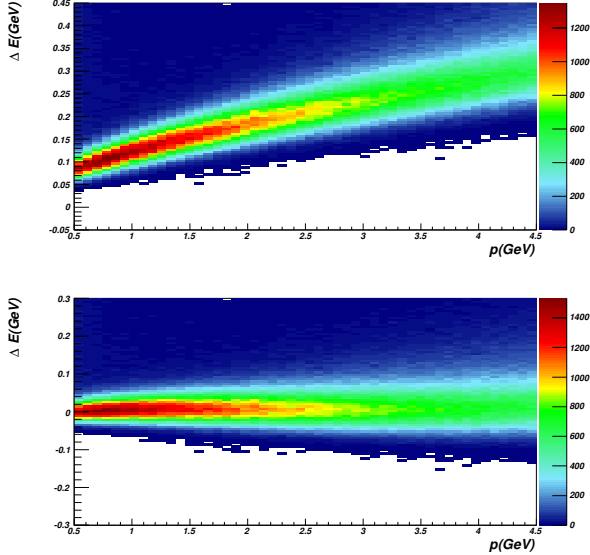


Figure 33: Top: difference between the simulated electron energy and the reconstructed cluster energy as a function of the electron energy for a 10 MeV equivalent threshold on the single crystal signal. Bottom: difference between the simulated electron energy and the cluster energy after the leakage correction.

1152 MeV: the leakage varies from  $\sim 80$  MeV (16%) for 500  
 1153 MeV electrons to  $\sim 300$  MeV (6.6%) for 4.5 GeV elec-  
 1154 trons.

1155 This effect can be easily corrected for by parametrizing  
 1156 the leakage as function of the reconstructed cluster  
 1157 energy and position and applying the correction in re-  
 1158 construction. In the specific case, simulations of single  
 1159 electrons were performed in GEMC and the difference  
 1160 between the reconstructed cluster energy and the elec-  
 1161 tron energy was studied as a function of the cluster seed  
 1162 crystal. For each crystal, the dependence of this differ-  
 1163 ence on the reconstructed cluster energy was fitted to a  
 1164 4th-order polynomial function which was then used as  
 1165 an additive correction to the reconstructed cluster en-  
 1166 ergy. The final dependence of the difference between  
 1167 corrected cluster energy and simulated energy is shown  
 1168 in the bottom panel of Fig. 33.

#### 1169 6.0.2. Electromagnetic background and radiation dose

1170 The electromagnetic background produced by the in-  
 1171 teraction of the electron beam in the target at the nom-  
 1172 inal CLAS12 luminosity was simulated in GEMC. For  
 1173 this purpose, in each event, about 124000, 11 GeV, elec-  
 1174 trons were generated originating 10 cm upstream the  
 1175 target. The electrons were distributed randomly with  
 1176 the radio-frequency structure of the CEBAF beam in a  
 1177 250 ns window. This number of electrons corresponds

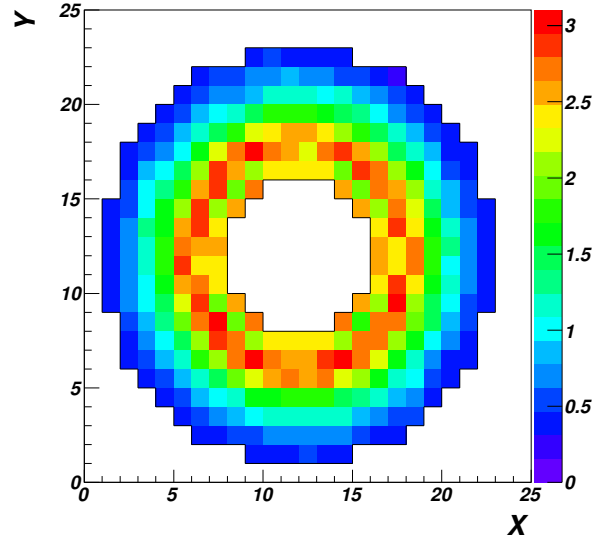


Figure 34: Radiation dose on the FT calorimeter crystals in rad/hour at  $10^{35} \text{ cm}^{-2} \text{s}^{-1}$  luminosity. The maximum values of about 5 rad/h are observed for the innermost crystals, i.e. at the smaller angles.

1178 to the number of beam electrons that would pass through  
 1179 the target in the chosen time window at the nominal  
 1180 CLAS12 luminosity of  $10^{35} \text{ cm}^{-2} \text{s}^{-1}$ . These simula-  
 1181 tions were used to study background rates in each of  
 1182 the FT detector, determine the pile-up probability and  
 1183 estimate the radiation dose the FT would be subject to  
 1184 during operations.

1185 The overall particle rate was found to be of about 120  
 1186 MHz, being dominated by very low energy particles and  
 1187 with only 6% due to particles with energy above 100  
 1188 MeV. In the energy range to be tagged (0.5-4.5 GeV)  
 1189 the overall particle rate is further reduced to about 180  
 1190 KHz, equally shared between photons and hadrons.

1191 For the FT-Cal, the energy deposition in each crys-  
 1192 tal was evaluated from the background simulation and  
 1193 used to calculate the dose per unit of time. The overall  
 1194 radiation dose at  $10^{35} \text{ cm}^{-2} \text{s}^{-1}$  was estimated to be less  
 1195 than 1.5 rad/h when averaged over the entire calorime-  
 1196 ter with a distribution on the calorimeter crystals as  
 1197 shown by Fig. 34. The maximum dose per crystal is of  
 1198 about 3 rad/h, which would result in an maximum inte-  
 1199 grated dose per crystal of about 2160 rad in 30 days of  
 1200 beam time.

1201 **7. Data reconstruction**

1202 **8. Detector performance**

1203 **9. Conclusions**

1204 **Acknowledgments**

1205 **References**

1206 **References**

1207 [1] G. M. B. Buonomo, P. Valente, Xxx, IEEE Trans. Nucl. Sci. 52  
1208 (2005) 824.